Chinese Journal of
POLYMER SCIENCE

RESEARCH ARTICLE

https://doi.org/10.1007/s10118-026-3751-1
Chinese J. Polym. Sci.

Boehmite/Polyacrylonitrile Composite Nanofiber Separator with Enhanced Ionic Conductivity and Thermal Stability for Lithium-Ion Batteries

Zhi-Jun Tu[a], Sheng-Bin Cao[a*], Xiao-Song Liu[b], Xiao-Peng Li[c], Wei Luo[c], and Dávid István Kis[d]

[a] *School of Materials, Shanghai Dianji University, Shanghai 201306, China*
[b] *Oxford Suzhou Centre for Advanced Research, Suzhou 215123, China*
[c] *College of Materials Science and Engineering, Donghua University, Shanghai 201620, China*
[d] *Department of Innovative Vehicles and Materials, GAMF Faculty of Engineering and Computer Science, John von Neumann University, Kecskemét 6000, Hungary*

Electronic Supplementary Information

Abstract Polyethylene (PE) and polypropylene (PP) are widely used in commercial lithium-ion battery (LIB) separators owing to their high mechanical strength and chemical stability. However, both polymers suffer from poor high-temperature tolerance, low porosity, and inadequate electrolyte wettability, making it difficult to reconcile electrochemical performance with safety under thermal stress. Developing advanced lithium-ion battery separators is therefore crucial for achieving high efficiency, safe LIBs. This study presents a boehmite/polyacrylonitrile (BM/PAN) composite nanofiber separator fabricated by electrospinning and systematically examines how BM loading affects separator microstructure and electrochemical behavior. Compared with commercial PP separators, the BM/PAN composites exhibit a unique three-dimensional interconnected fiber network, together with markedly improved wettability, thermal stability and electrochemical properties. The optimal formulation contains 4 wt% BM (denoted PAN-BM-4) exhibited an outstanding wettability with electrolyte uptake of 692.5% with the porosity of 80.7% and electrolyte contact angle of 25.5°, ensuring rapid electrolyte infiltration and efficient ion transport. It also displayed a higher mechanical property with tensile strength of 7.9 MPa and elongation at break of 27% (cf. 6.5 MPa and about 45% for pure PAN), indicating enhanced structural integrity. Meanwhile, such PAN-BM-4 separator demonstrates an excellent thermal stability with negligible shrinkage at 200 °C and a residual mass of 57.6% at 800 °C, effectively mitigating the thermal-runaway risk of conventional separators. Moreover, as to the electrochemical performance, this unique PAN-BM-4 separator showed an ionic conductivity of 3.31 mS/cm, more than six times that of commercial PP, and the electrochemical stability window exceeding 5.5 V (versus Li^+/Li) and a Li^+ transference number (t_{Li^+}) of 0.42, substantially higher than PP (0.28) and pure PAN (0.34), reflecting enhanced selective Li^+ transport. Besides, in half-cell testing, the PAN-BM-4 separator delivers an initial discharge capacity of 140.6 mAh/g at 0.5 C with 88.3% capacity retention after 100 cycles. In summary, this work establishes a viable materials-design strategy and experimental framework for next-generation LIB separators that simultaneously achieve high ionic conductivity, superior thermal stability and favorable interfacial compatibility.

Keywords Electrospinning; Lithium-ion battery; Separator; Polyacrylonitrile; Boehmite

Citation: Tu, Z. J.; Cao, S. B.; Liu, X. S.; Li, X. P.; Luo, W.; Kis, D. I. Boehmite/polyacrylonitrile composite nanofiber separator with enhanced ionic conductivity and thermal stability for lithium-ion batteries. *Chinese J. Polym. Sci.* https://doi.org/10.1007/s10118-026-3751-1

INTRODUCTION

Lithium-ion batteries (LIBs) have been widely adopted in electric vehicles and energy storage devices. Their excellent performance characteristics, including light weight, high energy density, and long cycle life, depend critically on the synergistic function of various core components.[1–4] These components primarily comprise the cathode, anode, electrolyte, and separator. Among them, the separator (aka diaphragm) serves a pivotal role by physically isolating the cathode and anode to prevent internal short circuits, while enabling free transport of lithium ions, providing guarantee for normal charging and discharging of the battery.[5,6] The failure of commercial polyolefin separators under high-temperature and high-rate conditions stems from intrinsic material limitations. Thermally, the low melting points of polyethylene (PE) (about 135 °C) and polypropylene (PP) (about 165 °C) cause severe shrinkage or rupture once overheated. Celgard 2400 (PP), for instance, exhibits noticeable shrinkage at 120 °C and, after 1 h at 180 °C, warps, discolors and shrinks by up to 88%.[7,8] Celgard 2325 (PP/PE/PP) incorporates a shutdown mechanism, yet its shutdown and rupture tempera-

* Corresponding author, E-mail: caosb@sdju.edu.cn
Received March 31, 2026; Accepted May 18, 2026; Published online August 18, 2026

tures are only 136.8 and 163.3 °C respectively; the narrow about 30 °C safety window is readily breached during thermal runaway, leading to internal short circuits.[9] Electrochemically, the non-polar backbone of polyolefins yields poor electrolyte wettability: Celgard 2400 has a contact angle of 66° and an electrolyte uptake of merely 102.8%, which promotes electrolyte dry-out in later cycles.[10] Its low porosity (41.5%) and poor wettability restrict ionic conductivity to 0.51 mS/cm, intensifying ohmic polarization during high-rate discharge and fostering non-uniform lithium dendrite growth.[11,12] The resulting Joule heat further elevates cell temperature, accelerating separator shrinkage and strength loss, which in turn facilitates dendrite penetration and ultimately triggers thermal runaway. To overcome these deficiencies, extensive research has produced advanced fabrication techniques including non-solvent induced phase separation (NIPS),[13] *in situ* covalent coupling[14] and electrospinning.[15] Among these, electrospinning has emerged as the leading platform because it yields nanofiber membranes with three-dimensional interconnected networks. The high porosity efficiently retains liquid electrolyte, thereby enhancing ionic conductivity and overall electrochemical performance. Precursor polymers such as poly(vinylidene fluoride) (PVDF),[16] PVDF-hexafluoropropylene (PVDF-HFP),[17] polyacrylonitrile (PAN)[18] and polyimide (PI)[19] have all been successfully demonstrated.

Polyacrylonitrile (PAN) is particularly attractive owing to its excellent spinnability and polar character. Its nanofiber network achieves porosities up to 71.2% with uniform pore-size distribution, substantially reducing lithium-ion transport tortuosity.[20] More importantly, PAN undergoes a cyclisation reaction at about 300 °C in air to form a trapezoidal heat-resistant structure. This transformation releases heat yet causes only minor fiber shrinkage rather than melting flow, preserving structural integrity above 200 °C.[21] This mechanism fundamentally eliminates the catastrophic shrinkage and short-circuits risk associated with thermoplastic polyolefins.

Boehmite (BM, *γ*-AlOOH) serves as an inorganic reinforcement phase. Its orthorhombic crystal structure (space group Cmc21, lattice parameters a=2.87 Å, b=12.23 Å, c=3.69 Å) confers excellent thermal stability and chemical inertness. Density-functional-theory calculations confirm that surface hydroxyl groups adsorb ethylene carbonate with an energy of −1.21 eV, markedly improving electrolyte wetting and retention.[22] Meanwhile, BM's low hardness avoids abrasive damage to the fibres while suppressing dendrite growth. When embedded in the PAN three-dimensional network, BM particles physically constrain thermal motion of PAN chains prior to cyclisation, and their surface —OH groups hydrogen-bond with PAN cyano groups (C≡N), synergistically enhancing dimensional stability and mechanical strength.[23]

Collectively, this composite system addresses polyolefin melt-shrinkage through PAN's cyclisation mechanism and overcomes poor wettability and dendrite penetration *via* BM's polar adsorption and low hardness, achieving a systematic improvement in thermal safety, electrochemical performance and mechanical stability from both molecular and structural perspectives. Based on the above analysis, this study incorporated boehmite (BM) nanoparticles into the polyacrylonitrile (PAN) electrospinning system. The BM/PAN composite nanofiber membranes with varying BM loadings were fabricated *via* the sol-gel-assisted electrospinning process, and the effects of BM content on fiber morphology, thermal stability, electrolyte affinity and electrochemical performance were systematically investigated to identify the optimal doping ratio. Lithium-ion batteries (LIBs) assembled with the optimized composite nanofiber membrane exhibited markedly improved impedance characteristics, cycling stability and rate capability.

EXPERIMENTAL

Materials and Reagents

Polyacrylonitrile (PAN, M_w=103 kDa, Huizhi Electric Textile Enter Enterprise Store, China), *N*,*N*-dimethylformamide (DMF, C_3H_7NO, 99.9%, Shanghai Aladdin Biochemical Technology Co., Ltd). Lithium iron phosphate electrode ($LiFePO_4$, Shenzhen Kejing Zhida Technology Co., Ltd), and boehmite (AlOOH) particles (average particle size 680 nm, 99.5%, Shanlin Stone Language Mineral Products Co., Ltd.) were used as received. The electrolyte was a 1.0 mol/L lithium hexafluorophosphate ($LiPF_6$) solution in a mixed solvent of dimethyl carbonate (DMC), diethyl carbonate (DEC), and ethylene carbonate (EC) at a 1:1:1 volume ratio (Suzhou Zhongyan Chemical Technology Co., Ltd.).

A commercial polypropylene (PP) membrane (Celgard 2400, thickness about 25 μm, producer) was employed as the reference separator. All reagents are of analytical grade and used without further purification unless otherwise specified.

Preparation of Pure PAN Nanofiber Membrane

The precursor solution was prepared *via* the sol gel method.[24] PAN powder was dissolved in DMF to prepare spinning solutions with mass fractions of 12%, 14%, and 16%, respectively. The mixed solution was placed in a constant-temperature water bath of 60 °C and magnetically stirred for 4 h, followed by ultrasonic oscillation for 1 h to obtain a uniform, transparent, pale-yellow precursor solution (Fig. 1). After static defoaming for 12 h, electrospinning was performed using the following parameters: DC voltage of 15 kV, feed rate of 0.8 mL/h, collector drum speed of 1000 r/min, tip-to-collector distance of 15 cm, ambient temperature of (25±2) °C, relative humidity of 40%±5%. The as-spun fiber membranes were vacuum-dried at 60 °C for 4 h to remove residual solvent.

Preparation of BM/PAN Composite Nanofiber Membrane

Boehmite (BM) powder with mass fractions of 2%, 4%, and 6% was ground for 30 min and subsequently added to certain amount of DMF. The mixture was subjected to ultrasonic vibration for 2.5 h in constant-temperature water bath at 60 °C to ensure uniformly dispersion of BM powder in DMF without visible particle precipitation, yielding a stable BM/DMF dispersion. For the preparation of BM/PAN composite spinning solutions, the BM dispersions of varying concentrations were mixed with the optimal PAN solution at predetermined ratios. The mixtures were further ultrasonicated at 80 °C for 1.5 h to achieve uniform dispersion of BM within the PAN solution, forming a series of BM/PAM composite electrospinning solutions (Fig. 1). After defoaming, electrospinning was conducted using identical parameters as described in **Preparation of Pure PAN Nanofiber Membrane** section. The prepared composite nanofiber mem-

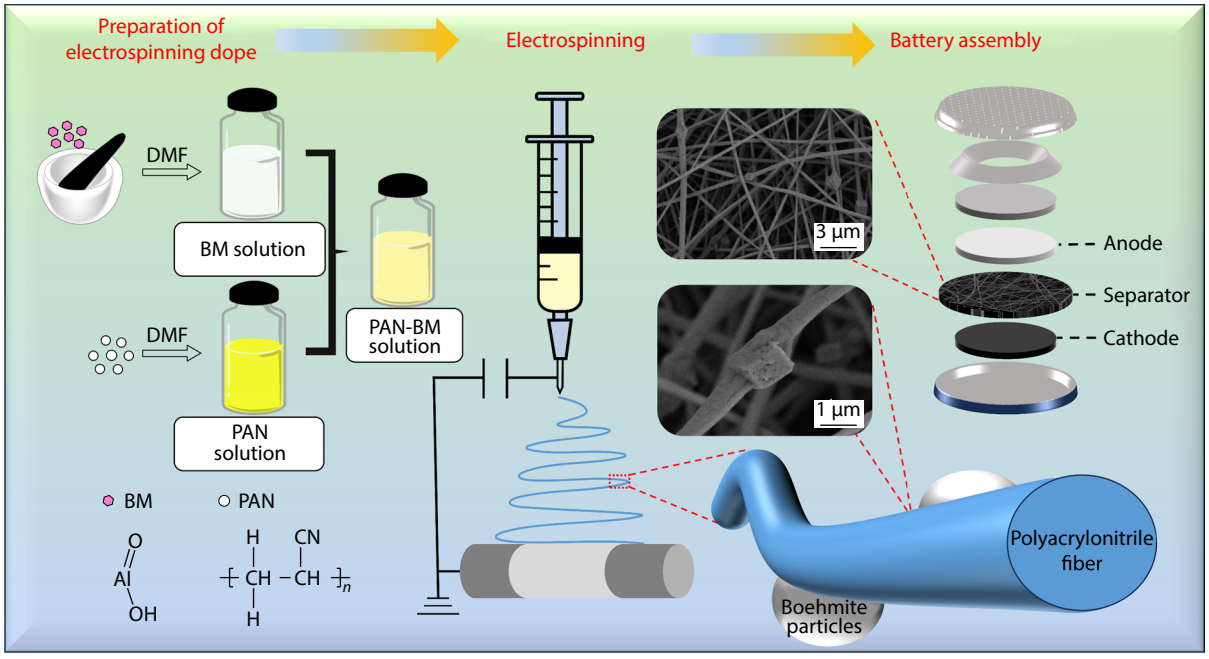

Fig. 1 Schematic diagram of the fabrication of boehmite (BM)/polyacrylonitrile (PAN) composite nanofiber separators and their application in lithium-ion batteries.

branes were drying in a vacuum oven at 60 °C for 4 h, and the resulting samples were named PAN-BM-*x* (*x*=20, 35, 50, representing the mass fraction of boehmite (BM) nanoparticles in PAN).

Characterizations

Structure and morphology analysis

The surface morphology of the membrane was examined using a field emission scanning electron microscope (FE-SEM, Zeiss Merlin Compact, Germany) at an acceleration voltage of 5 kV and gold spraying treatment for 30 seconds prior to capture images. Fiber diameters were measured by randomly selected 100 fibers were using Image J software.

Fourier transform infrared spectroscopy (FTIR, VERTEX 70, USA) was employed to analyze the surface functional groups in the range of 400–4000 cm^{-1}, with a resolution of 4 cm^{-1}.

X-ray diffraction (XRD, D8 ADVANCE, Germany) was used to characterize the crystal structure using Cu*Kα* radiation (*λ*=0.154 nm) at 40 kV and 40 mA with a scanning range of *2θ* from 10° to 70° at a rate of 5 (°)/min.

Thermal performance analysis

Thermal performance was evaluated using a synchronous thermal analyzer (TG-DSC, NETZSCH STA 509 Jupiter, Germany). Samples (about 5 mg) were placed in an alumina crucible and heated from 20 °C to 800 °C at a heating rate of 10 °C/min under an argon atmosphere. Heat resistance was assessed based on the melting endothermic peak in the differential scanning calorimetry (DSC) traces obtained simultaneously, while the initial decomposition temperature and residual mass were determined from the TG curve.

The thermal dimensional stability of the separator film is quantitatively evaluated by measuring the change in its area before and after high-temperature treatment, according to Eq. (1),[25]

$$\text{Thermal shrinkage}\,(\%) = \frac{A_0 - A}{A_0} \times 100 \quad (1)$$

where A_0 and A stand for the surface area of the separator film before and after thermal treatment, respectively.

Mechanical performance testing

The mechanical performance of the prepared nanofiber membrane was characterized using a fiber tensile strength tester (Shanghai Chenhua Instrument Co., Ltd. XWW-20A universal testing machine, China). The membrane was cut into specimen strips of 10 mm × 50 mm and tested at a tensile speed of 20 mm/min with a clamping distance set at 20 mm. The stress-strain curve during the tensile process was recorded and the averaged value of five tests was reported hereby.

Porosity and Electrolyte Wettability Evaluations

The porosity of the membrane was measured by using *n*-butanol liquid absorption method. Membranes were cut into circular pieces (diameter=19 mm), vacuum-dried at 60 °C for 12 h, and weighed to obtain the dry mass (M_d). The membranes were then immersed in *n*-butanol for 2 h, removed, gently wiped with filter paper to remove excess surface liquid, and reweighed to obtain the wet film (M_w). Porosity was calculated using Eq. (2),[26]

$$P\ (\%) = \frac{M_w - M_d}{\rho V_d} \times 100 \quad (2)$$

where, P is the porosity (%), M_w and M_d are wet and dry membrane masses (g), respectively, and ρ is the density of *n*-butanol (g/cm^3) and V_d is the volume of the dry membrane (cm^3).

The electrolyte contact angle (drop volume = 3 μL) was measured using a contact angle goniometer (Kruss DSA 100, Germany) to quantitatively evaluate the surface wettability. Measurements were performed at a minimum of five different locations per sample, and ImageJ was used to calculate the angle between the electrolyte droplet and the membrane surface, and then the average value was reported.

https://doi.org/10.1007/s10118-026-3751-1

For electrolyte uptake measurement, a predetermined mass of dry membrane was immersed in electrolyte for 2 h, then removed. Excess electrolyte was gently wiped from the surface with filter paper, and the membrane was reweighed. All tests were conducted in an argon-filled glove box. The electrolyte uptake (EU) was calculated using Eq. (3),[27]

$$\mathrm{EU}\,(\%) = \frac{W_1 - W_0}{W_0} \times 100 \tag{3}$$

where W_0 and W_1 represent the mass of the dry membrane and the electrolyte-saturated membrane, respectively.

Electrochemical performance analysis

The ionic conductivity of the membrane was determined by electrochemical impedance spectroscopy (EIS). Membranes were cut into circular samples (diameter 19 mm) and assembled into a stainless steel (SS)/membrane/stainless steel (SS) symmetric cell in an argon-filled glove box (H_2O<0.1 cm^3/m^3, O_2<1 cm^3/m^3) with appropriate electrolyte addition. The cells were assembled in CR2032 coin cell cases and allowed to equilibrate for 12 h prior to testing. The alternating current (AC) impedance measurements were performed at room temperature using an electrochemical workstation (CH Instruments, USA) in a two-electrode configuration, with a frequency range of 100 mHz to 1 MHz and amplitude of 5 mV. The bulk resistance (R_b) was determined from the intercept of the high-frequency semicircle with the real axis, and ionic conductivity (σ) was calculated using Eq. (4),[28]

$$\sigma = \frac{d}{R_b \times S} \tag{4}$$

where d is the membrane thickness (μm), S is the effective membrane area (cm^2), and R_b is the bulk impedance (Ω).

To eliminate the impact of membrane thickness differences on the evaluation of ion transport performance, the area-specific resistance (ASR) is used for a thickness-independent fair comparison. According to the definition of ionic conductivity as shown in Eq. (4) and ASR (Ω·cm^2) is expressed as shown in Eq. (5), representing the total ionic transport resistance per unit area of the membrane. A lower ASR value indicates a smaller actual hindrance for ions passing through the membrane.

$$\mathrm{ASR} = R_b \times S = \frac{d}{\sigma} \tag{5}$$

where R_b is the bulk resistance (Ω) obtained from the Nyquist plot, d is the thickness of the membrane (cm), and S is the effective geometric area of the stainless-steel electrode (electrode diameter 15.6 mm, S ≈ 1.91 cm^2).

The electrochemical stability window was evaluated by linear sweep voltammetry (LSV). The membrane was sandwiched between a stainless steel (SS) working electrode and a lithium counter/reference electrode. Cell assembly was conducted in an argon-filled glove box. LSV measurements were performed at room temperature from 2 V to 6 V at a scan rate of 5 mV/s. The electrochemical stability window is defined as the potential corresponding to an anodic current density of 0.05 mA/cm^2. Based on the geometric area of the stainless-steel electrode (diameter 15.6 mm, S ≈ 1.91 cm^2), the original current corresponding to this cutoff current density is approximately 0.096 mA.

The lithium-ion transference number (t_{Li^+}) was measured using a combination of AC impedance (EIS) and DC polarization (*I-t*) techniques. During the test, a separator soaked with liquid electrolyte was placed between two lithium metal sheets to assemble a Li||Li symmetric coin cell. The lithium-ion transference number (t_{Li^+}) was calculated using the following Eq. (6),[29]

$$t_{Li^+} = \frac{I_s\,(V - I_0 R_0)}{I_0\,(V - I_s R_s)} \tag{6}$$

where I_0 and I_s are the initial current before polarization and the steady-state current after polarization, respectively. R_0 and R_s are the battery interface resistances before and after polarization, respectively. V is the applied step potential.

Cycle and rate performance testing

Half-cells were assembled in an argon-filled glove box using $LiFePO_4$ as the cathode and lithium metal as anode. The separator was cut into circular sample (diameter 19 mm), placed between the electrodes, and wet with appropriate electrolyte. The cell was packaged in a CR2032 battery coin cell case and sealed tightly using a coin cell crimper (MSK-10, China). The sealed cells were removed from glove box and allowed to rest at room temperature for 24 h to ensure complete electrolyte infiltration into the separator and electrodes.

Cycling and rate performance tests were conducted using a battery cycler (CT-4008T-5V20mA-S4, Neware, China) with a voltage range of 3.0–4.2 V. Cells were initially subjected to formation cycling at a low rate of 0.1 C/0.1 C, followed by 100 charge-discharge cycles at a rate of 0.5 C to evaluate cycling stability. For rate capability testing, cells were charged at a rate of 0.1 C and discharged at progressively increasing rates of 0.2, 0.5, 1, 2, and finally returned to 0.2 C, with five cycles at each rate.

RESULTS AND DISCUSSION

Morphology Analysis

Fig. 2 presents SEM images and corresponding fiber diameter distributions of electrospun nanofiber membranes prepared at varying PAN concentrations and BM doping levels. For pure PAN fiber membranes (Figs. 2a–2c), at 12 wt% PAN, the fibers exhibited smooth surface with uniform diameter (462.9±13.4 nm), and no inter-fiber adhesion (Fig. 2a). As the concentration increased to 14 wt% and 16 wt%, the average fiber diameter increased to (523.8±5.1) nm and (707.0±7.7) nm, respectively, with severe fiber adhesion and agglomeration observed in the 16 wt% sample (Fig. 2c). This phenomenon arises from the significant increase in viscosity of the spinning solution at higher polymer concentrations, which weakens the electric field stretching of the jet during the electrospinning. Concurrently, reduced jet stability leads to fiber adhesion.[30] Based on the comprehensive evaluation of fiber morphology, diameter uniformity, and membrane structural integrity, PAN-12 was selected as the base matrix for subsequent BM doping.

Upon introducing BM nanoparticles (Figs. 2d–2f), PAN-BM-20 (20 wt% BM) fibers remained smooth surfaces with only sparse BM particle distribution (Fig. 2d). PAN-BM-35 (35 wt% BM) exhibited both smooth fiber surfaces and uniform BM particles distribution throughout the fibers and membrane, with an average fiber diameter of (320.15±5.74) nm (Fig. 2e). In contrast, PAN-BM-50 (50 wt% BM), despite further reduced fiber diameter (270.98±3.38 nm), displayed partial fiber frac-

ture and structural damage (Fig. 2f). These changes can be attributed to the fact that at low BM doping levels, nanoparticles refine the fibers by reducing the apparent viscosity of the spinning solution and enhancing the jet stretching,[31] while maintaining good compatibility with the PAN matrix. However, at high doping levels, excessive particle aggregation and stress concentration compromise fiber structural integrity. Hereby, 12 wt% PAN is the optimal matrix concentration, and 35 wt% BM doping yields membranes with uniform morphology and intact structure, providing a crucial morphological foundation for the subsequent development of high-performance lithium-ion battery separators.

Chemical Composition and Crystal Structure

The Fourier transform infrared spectroscopy (FTIR, Figs. 3a–3c) revealed characteristic absorption peaks for all samples. The stretching vibration of cyano group (—C≡N) at 2243 cm^{-1} confirms the intact main structure of PAN molecular chains. The peak at 1079 cm^{-1} is attributed to the ether bond (C—O—C) vibrations, while characteristic peaks at 745 cm^{-1} and 617 cm^{-1} correspond to the Al-O bond vibration of boehmite, indicating successful incorporation of BM into the PAN matrix.[32]

X-ray diffraction (XRD, Figs. 3d–3f) analysis identified the characteristic diffraction peaks of BM at 2θ=14.482°. The measured diffraction patterns were respectively matched and compared with the standard PDF card of PAN (PDF#00-048-2119) and of boehmite (PDF#98-000-0120) to complete phase identification as noted in Fig. 3(d). Pure PAN samples exhibited a broad amorphous halo centered at 2θ=16.7°, characteristic of the disordered structure of PAN molecular chains.[33] For pure PAN systems, as concentration increases from 12% to 16%, the intensity of PAN characteristic peaks gradually decreases with reduced full width at half maximum (FWHM), though peak shapes remain broad. However, SEM characterization revealed that 16% PAN caused severe fiber adhesion due to high solution viscosity, compromising membrane performance.

In the BM doped systems, as BM content increased from 20% to 50%, PAN characteristic peak intensity progressively decreased with synchronous reduction in FWHM, while peak shape remains broad yet became more defined. This indicates that BM nanoparticles induce more regular arrangement of PAN molecular chains through physical interactions.[34] The BM characteristic peak intensity remained stable from 20% to 35%, but decreased significantly at 50% BM, highly consistent with SEM-observed fiber fracture and particle aggregation at this doping level (Fig. 2f), confirming that excessive BM causes diffraction signal dispersion due to aggregation effect.

Although 16% PAN exhibited improved molecular chain regularity, severe fiber adhesion obstructs pore channels, reducing porosity and electrolyte permeability, thereby compromising the essential ion transport function of lithium-ion battery separators. In contrast, 12% PAN, despite slightly lower molecular chain regularity, forms smooth fibers without bead-like defects or adhesion, creating a continuous, uniform three-dimensional porous network structure that ensures adequate electrolyte infiltration and rapid lithium-ion transport. More importantly, with BM doping, the 12% PAN matrix not only enhances molecular chain regularity through particle action but also maintains excellent porous structure. At 35% BM, particles are uniformly dispersed without aggregation-induced structural damage. Therefore, considering porous structure integrity, ion transport efficiency, and doping modification stability, 12% PAN serves as the optimal matrix for constructing high-performance separators, with 35% BM identified as the optimal doping level.

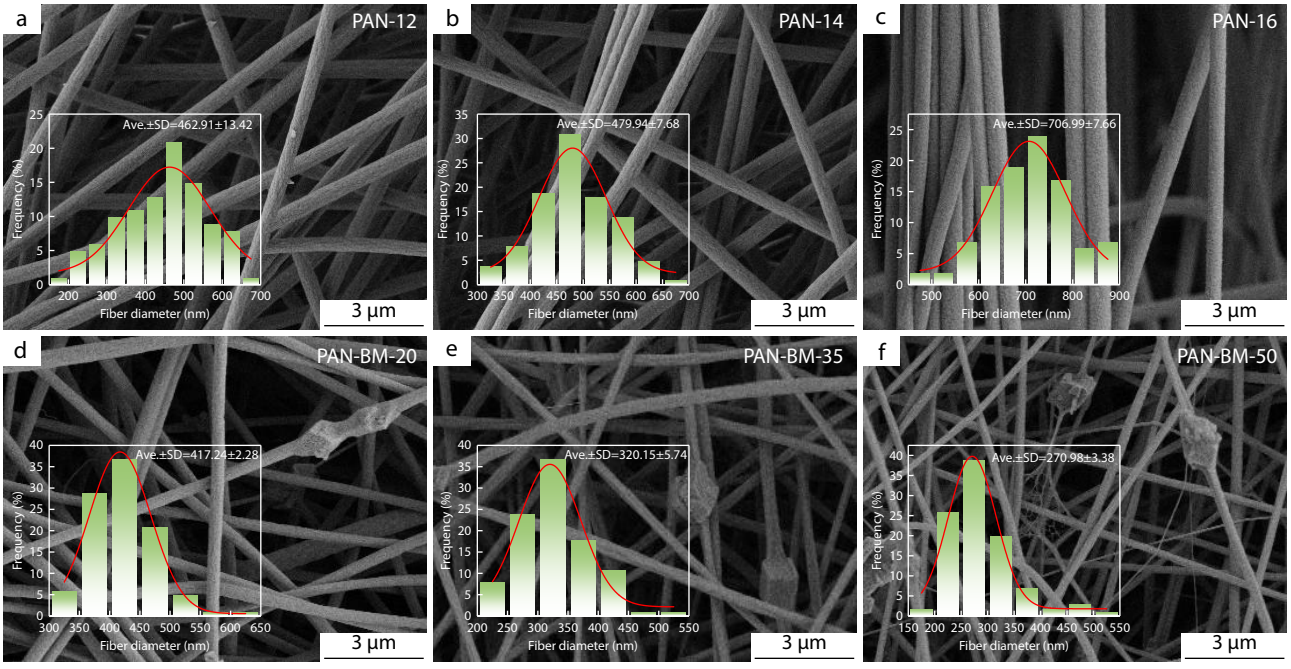

Fig. 2 SEM images and corresponding fiber diameter distribution of electrospun PAN based fiber membranes with (a–c) different PAN concentrations and (e–f) boehmite (BM) doping levels: (a) 12 wt% PAN, (b) 14 wt% PAN, (c) 16 wt% PAN, (d) PAN-BM-20, (e) PAN-BM-35, and (f) PAN-BM-50.

https://doi.org/10.1007/s10118-026-3751-1

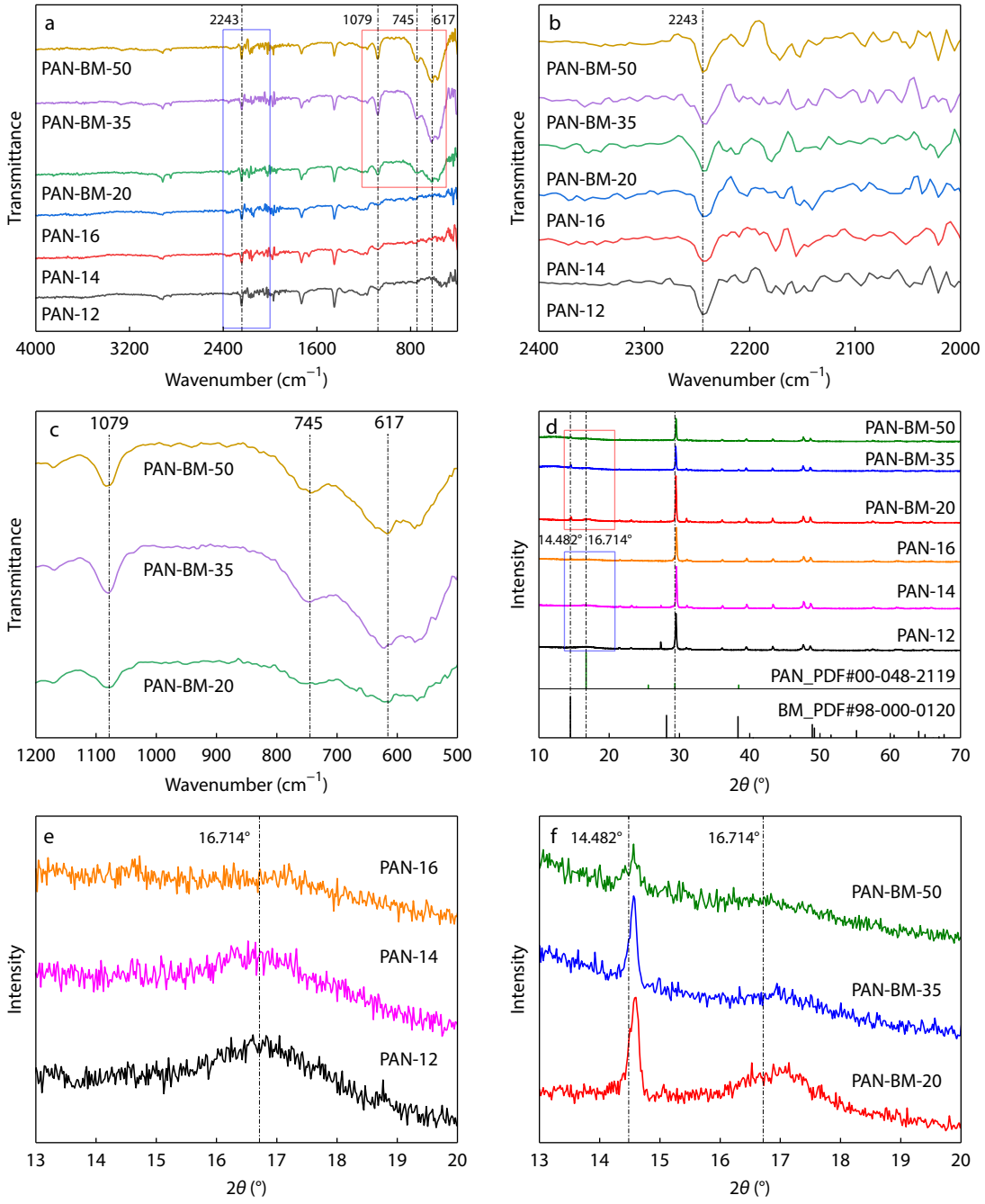

Fig. 3 (a–c) FTIR spectra and (d–f) XRD patterns of electrospun PAN based fiber membranes with different PAN concentrations and boehmite doping levels.

Wetting Kinetics and Electrolyte Penetration

The porosity, electrolyte uptake, and contact angle of separators are critical parameters for evaluating electrolyte affinity. As shown in Figs. 4(a) and 4(b), commercial Celgard 2400 membrane exhibits a porosity of merely 41.5%, electrolyte uptake of 114.1% and a contact angle as high as 44.9°. These limitations arise from its narrow slit-shaped pores formed by dry stretching and the inherently non-polar surface of the polyolefin material. In market contrast, all electrospun PAN-based membranes display three-dimensional porous structure with porosities exceeding 72%.[35] Within the pure PAN system, the 12 wt% PAN membrane achieved a porosity of 84.9% and electrolyte uptake of 545.3%, both significantly surpassing those of the 14 wt% and 16 wt% samples. The 16 wt% PAN samples exhibited reduced porosity (72.5%) and electrolyte uptake (433.1%) due to severe fiber adhesion obstructing pore channels. Upon BM doping, electrolyte uptake displayed a volcanic-shaped trend, initially increasing and then decreasing. The PAN-BM-35 membrane reached a peak uptake of 692.5%, representing a 27.0% increase over pure PAN-12, while PAN-BM-50 declined to 580.2%. This indicates that optimal BM content synergistically enhances the electrolyte absorption capacity through the hy-

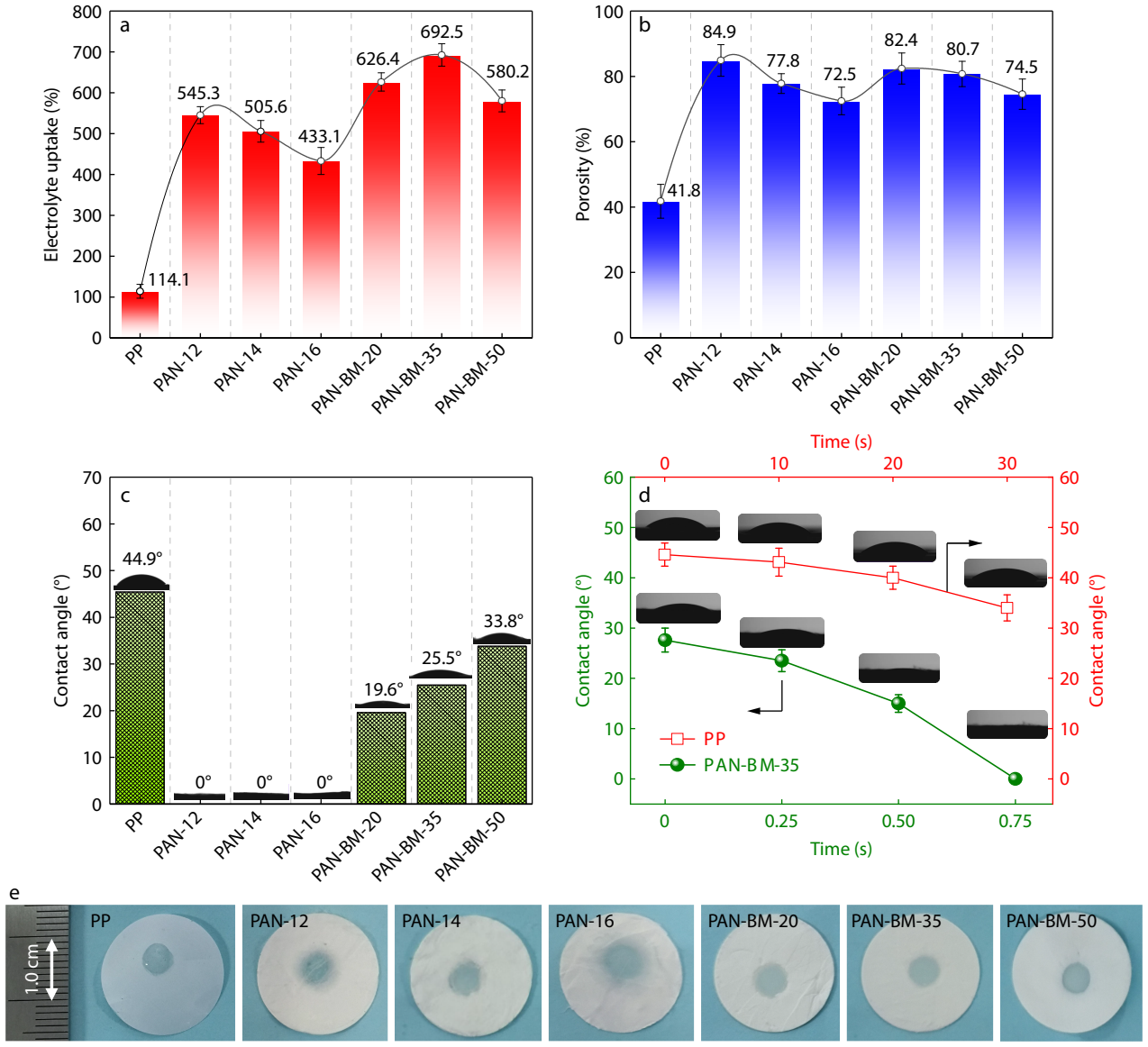

Fig. 4 Properties of commercial PP and electrospun PAN-based membranes: (a) electrolyte uptake, (b) porosity, (c) electrolyte contact angle, (d) dynamic wetting and spreading on PP and PAN-BM-35 surfaces, (e) optical images of actual electrolyte wetting on membranes.

drophilic effect of surface hydroxyl groups and uniform porous structure. However, excessive BM induces particle aggregation, disrupting pore continuity and reducing electrolyte uptake.[36]

Contact angle measurements (Fig. 4c) further corroborate these findings. The 12 wt% PAN membrane exhibited a contact angle of 0°. The contact angle results in Fig. 4(c) show that the contact angles of 12 wt%, 14 wt%, and 16 wt% PAN membranes are all 0°, achieving complete electrolyte wetting. Although PAN-BM-35 displayed a slightly elevated contact angle of 25.5° following BM doping, this value remains substantially lower than the 44.9° of PP membrane.

The dynamic wetting and penetration kinetics of the prepared membrane with liquid electrolyte were characterized through contact angle measurements, with results presented in Fig. 4(d). The commercial PP membrane exhibits an initial electrolyte contact angle of approximately 44.9°, indicating poor intrinsic affinity with the polar electrolyte. After 30 seconds, the contact angle decreases only marginally to 34°, with no observable droplet spreading or penetration, demonstrating extremely sluggish wetting kinetics. In marked contrast, the PAN-BM-35 membrane displays an initial contact angle of merely 27.6°, signifying superior intrinsic wettability. The contact angle rapidly diminishes to 0° within 0.75 seconds, with complete electrolyte spreading and penetration into the membrane's porous skeleton, achieving ultrafast electrolyte infiltration at a rate exceeding 40 times that of the commercial PP membrane. However, the PAN-BM-35 membrane displays an apparently paradoxical wetting behavior: its initial contact angle is 25.5°, higher than the near-0° value of the pure PAN-12 membrane, yet the electrolyte droplet fully penetrates and vanishes within 0.75 s (Fig. 4d). This can be explained by the synergistic interplay between BM-induced surface chemistry and microstructure.

Chemically, BM particles partially coat the PAN fibers, and

the exposed Al-OH groups are less polar than the native —C≡N groups, lowering the surface energy from strongly hydrophilic to moderately hydrophilic. Physically, BM nanoparticles create nanoscale protrusions that substantially increase surface roughness. Szewczyk *et al*. demonstrated that for electrospun fiber mats, surface geometry (roughness) rather than chemical composition is the dominant determinant of the apparent contact angle.[37] In the present system, the increased roughness prevents the droplet from fully wetting the nanoscale grooves upon initial contact, so the droplet remains in a partially non-wetted state, and the apparent angle stabilizes at 25.5°. Simultaneously, the three-dimensional interconnected network (porosity 80.7%) provides abundant through-channels; capillary action rapidly draws the electrolyte into the membrane bulk, completing full infiltration in 0.75 s.[38] Thus, the 25.5° contact angle does not signify poor wettability but rather reflects an optimised balance of surface chemistry and pore architecture, attesting to the excellent electrolyte affinity of the PAN-BM composite membrane.

The photographs in Fig. 4(e) visually demonstrate the wetting behavior of different membranes. On commercial Celgard PP, electrolyte forms discrete droplets, indicating slow electrolyte diffusion and poor wettability. In contrast, electrolyte rapidly spreads and complete infiltrates the PAN-12 membrane surface without visible residue, visually confirming its exceptional hydrophilicity with a 0° contact angle. The PAN-BM-35 surface also exhibits rapid electrolyte spreading with only a thin liquid film at the edges, indicating that moderate BM doping preserves membrane hydrophilicity. However, small droplet residues appear on PAN-BM-50, attributed to surface irregularities caused by excessive BM aggregation.

Electrochemical Performance

The electrochemical characterization results in Fig. 5 comprehensively reveal the ion transport characteristics and interfacial stability of different separators. In the electrochemical impedance spectrum (EIS) shown in Fig. 5(a), the intersection of the high-frequency semicircle with the real axis corresponds to the bulk resistance R_b. The calculated ionic conductivity (δ, mS/cm) and area-specific resistance (ASR, Ω·cm^2) are summarized in Table 1. The commercial PP separator exhibits an R_b of 2.88 Ω and an ion conductivity of merely 0.31 mS/cm. The pure PAN-12 membrane shows reduced R_b of 1.19 Ω and enhanced ion conductivity of 2.08 mS/cm, directly attributed to its high porosity, open pore structure, and excellent electrolyte wettability. The PAN-BM-35 membrane further reduced R_b to 0.72 Ω, achieving an ion conductivity of 3.31 mS/cm, which is about 10.7 times that of the PP and 1.6 times that of the pure PAN-12 membrane. This conductivity level ranks among the highest re-

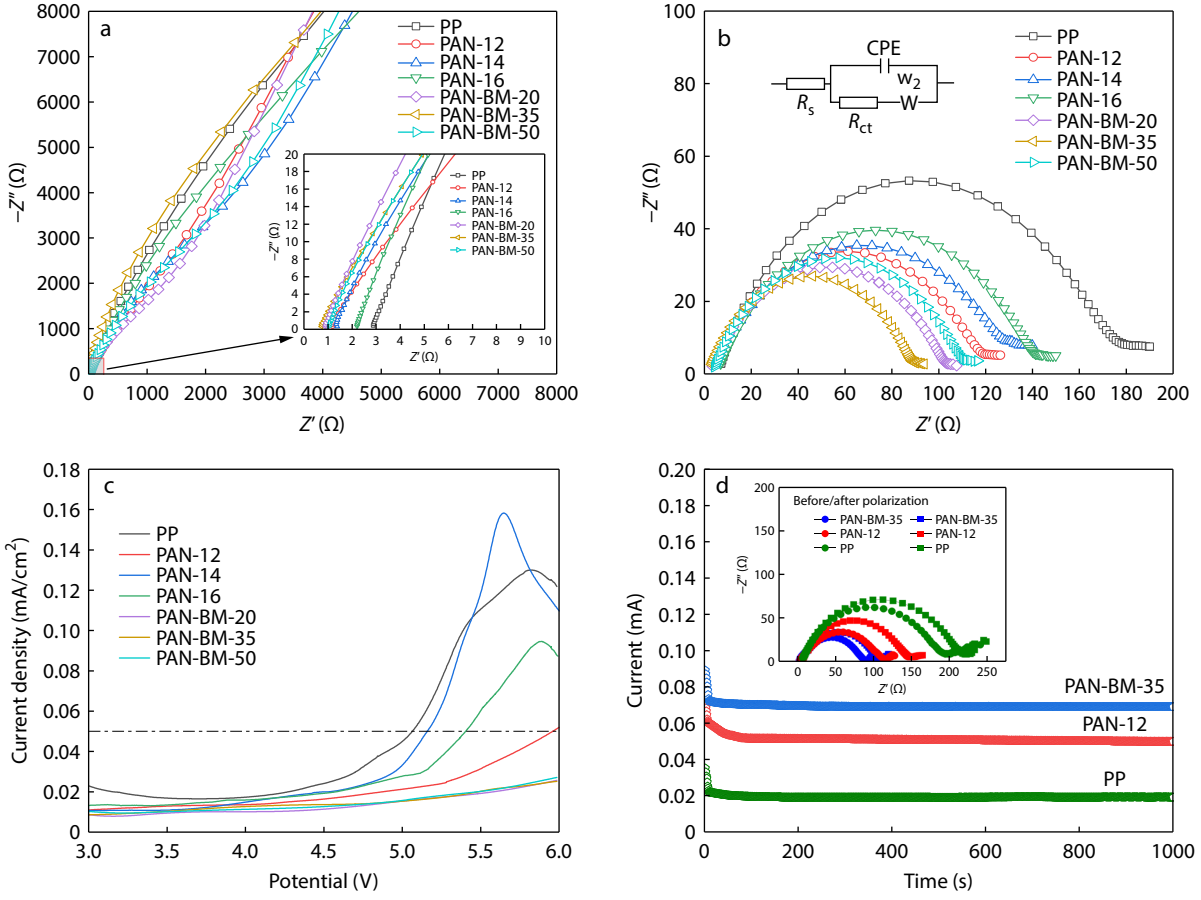

Fig. 5 AC impedance and electrochemical stability of cells with different separators: (a) stainless steel (SS)/separator/SS cells and interfacial resistances, (b) Li/separator/Li cells; (c) Linear sweep voltammetry (LSV) traces of SS/separator/Li cells (dashed line indicates the cutoff threshold of 0.05 mA/cm^2), and (d) electrochemical impedance spectra of Li/diaphragm/Li cells before and after polarization.

https://doi.org/10.1007/s10118-026-3751-1

Table 1 Physical characteristics and electrochemical performance of commercial celgard and PAN nanofiber membranes.

Separator	Thickness (mm)	R_b (Ω)	δ (mS/cm)	ASR (Ω·cm^2)
PP	0.025±0.002	2.88	0.31	5.50
PAN-12	0.070±0.002	1.19	2.08	2.27
PAN-14	0.070±0.003	1.38	1.79	2.64
PAN-16	0.068±0.002	2.20	1.09	4.20
PAN-BM-20	0.070±0.005	0.89	2.76	1.71
PAN-BM-35	0.068±0.005	0.72	3.31	1.38
PAN-BM-50	0.066±0.005	1.04	2.24	1.99

ported for electrospun PAN-based composite membranes, attributed to: (1) surface hydroxyl groups on BM particles enhancing electrolyte affinity and effective electrolyte retention; (2) uniformly dispersed BM nanoparticles forming ion-conductive bridges within the PAN matrix, providing additional lithium-ions transport pathways; (3) the three-dimensional interconnected nanofiber network offering continuous, low-tortuosity channels for ion migration.[39]

Fig. 5(b) presents the charge transfer resistance (R_{ct}) values obtained from EIS fitting. The PP separator exhibits a high R_{ct} of 182.3 Ω, indicating poor electrode-electrolyte interfacial contact. The pure PAN-12 membrane reduces R_{ct} to 121 Ω, while PAN-BM-35 further decreases it to 87 Ω, a reduction of 46.4%. This diminished interface impedance mitigates lithium-ion accumulation at the electrode/separator interface and suppresses lithium dendrite nucleation and growth. Excessive BM doping (50 wt%) increases R_{ct} to 112 Ω, directly associated with fiber fracture and interfacial heterogeneity induced by particle aggregates.

The electrochemical stability of the membranes under oxidative conditions was evaluated by linear sweep voltammetry (LSV) with the corresponding results are shown in Fig. 5(c). A current-density threshold of 0.05 mA/cm^2 was adopted as the onset of electrolyte decomposition. Commercial PP separators begin to decompose at about 5.0 V (versus Li^+/Li). The PAN-16 and PAN-14 membranes extend this limit to about 5.1 V and 5.4 V respectively, whereas the PAN-12 membrane achieves a substantially wider window of 5.9 V. Notably, all BM-doped membranes (PAN-BM-20, PAN-BM-35 and PAN-BM-50) maintain current densities below the cutoff throughout the entire scan up to 6.0 V, indicating that their anodic stability exceeds the instrument limit. This superior performance is attributed to the excellent electrolyte-retention capacity of the composite, which suppresses local electrolyte depletion and associated oxidative decomposition at high potential. Uniformly dispersed BM nanoparticles, with their intrinsic chemical inertness and high specific surface area, further stabilise the electrode–electrolyte interface and retard its degradation.[40]

The lithium-ion transference number (t_{Li^+}) was measured by the Bruce-Vincent method, and the corresponding chronoamperometry curves and impedance spectra before and after polarisation are shown in Fig. 5(d). The PAN-BM-35 membrane achieves t_{Li^+}=0.42, a 50% increase over commercial PP (0.28) and a 24% increase over pure PAN-12 (0.34). This enhancement arises from three synergistic factors. First, the high porosity (80.7%) and three-dimensional interconnected nanofibre network provide abundant, low-tortuosity channels for Li^+ transport, shortening the effective diffusion distance and accelerating ion migration. Second, the high electrolyte uptake (692.5%) ensures sufficient electrolyte retention within the porous structure, maintaining a continuous Li^+ supply and alleviating concentration polarization at the electrode-electrolyte interface. Third, surface hydroxyl groups (—OH) on BM nanoparticles hydrogen-bond with PF_6^- anions, effectively immobilizing some anions and promoting preferential Li^+ transport. This selective anion anchoring, combined with physically enhanced ion transport, enables the membrane to deliver both high-flux Li^+ conduction and improved Li^+ selectivity.[41]

Thermal Stability and Flame Retardancy Analysis

Under overcharge, short-circuit, or high-temperature conditions, lithium-ion battery separators must withstand extreme temperatures without significant thermal shrinkage or structural damage, preventing direct contact between electrodes that could trigger thermal runaway. Consequently, thermal stability represents a critical safety indicator for battery performance.[42] Hereby, the thermal dimensional stability was assessed by exposing separators to elevated temperatures. As shown in Fig. 6(a), commercial Celgard PP undergoes severe curling and melting after 30 min at 200 °C, with an area shrinkage exceeding 95% and complete loss of structural integrity. The pure PAN membrane does not melt under the same conditions but exhibits obvious warping. By contrast, all BM-doped PAN composites retain their shape with negligible curling and an area shrinkage below 3%. When the temperature is raised to 250 °C, pure PAN warps significantly (area shrinkage 24.6%). The BM-doped composites also deform, yet to a markedly lesser degree: area shrinkage falls to 19.9%, 15.2% and 10.2% for PAN-BM-20, PAN-BM-35 and PAN-BM-50 respectively, with PAN-BM-50 showing a nearly 60% reduction relative to the pure PAN system. Although the boehmite inorganic framework cannot fully suppress thermal deformation of the PAN matrix at extreme temperatures, it effectively restricts chain mobility through physical confinement, rendering the composite separators substantially more dimensionally stable than their pure PAN counterpart.[43]

Fig. 6(b) presents visual ignition test results. The PP separator ignites rapidly and burns vigorously within 1 s, while combustion of the 12 wt% PAN separator proceeds significantly slower. The PAN-BM-35 separator demonstrates the longest combustion delay, indicating that BM nanoparticles effectively suppress flame propagation and enhance flame retardancy.[44] These experiments preliminarily confirm that PAN/BM nanofiber membranes possess superior high-temperature resistance and flame-retardant potential compared to commercial PP membranes. To further quantify thermal stability, differential scanning calorimetry (DSC) and thermogravimetric analysis (TGA) were performed. Fig. 6(c) shows a pronounced melting endotherm for the PP membrane at 166.3 °C, corresponding to its thermal runaway onset temperature. In contrast, PAN-based membranes exhibit melting/decomposition peaks above 300 °C, with PAN-BM-35 peaking at 301.9 °C, slightly higher than pure PAN-12 (300.8 °C), confirming that BM doping enhances thermal stability and delays thermal decomposition.

TGA results (Fig. 6d) indicate complete PP decomposition

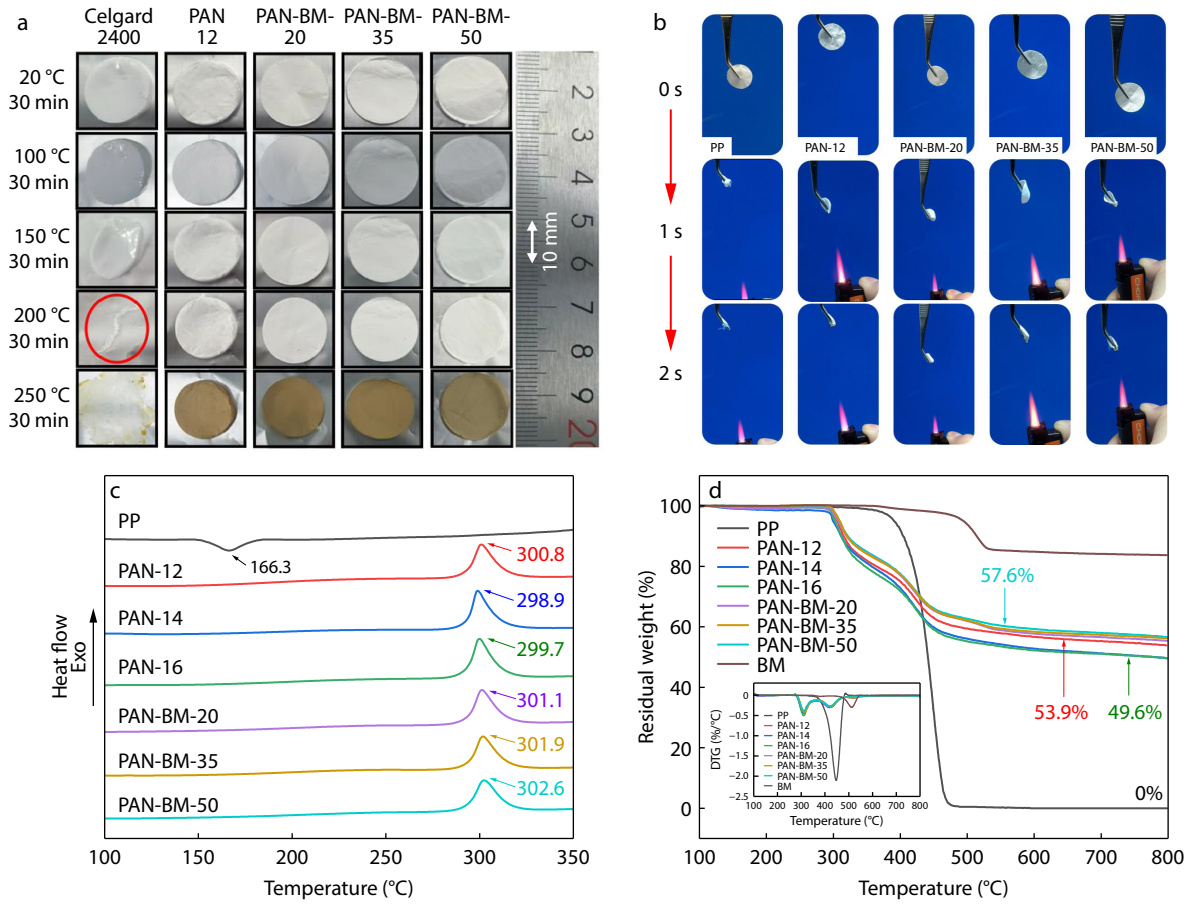

Fig. 6 (a) Dimensional stability after thermal treatment at various temperatures, (b) photographs during ignition tests, (c) differential scanning calorimetry (DSC) and (d) thermogravimetric analysis (TGA) traces.

near 460°C (0% residual mass), whereas PAN-based membranes retain significant residue at 800°C: PAN-12 shows 53.9% residual mass, while PAN-BM-50 further increases to 57.6%. This demonstrates that elevated BM content reduces thermal decomposition product release and improves thermal stability.[45] Based on comprehensive thermal shrinkage, combustion behavior, and thermal analysis results, the 12 wt% PAN matrix with 35 wt% BM doping achieves synergistic optimization of low shrinkage, slow combustion, and high thermal residue, providing exceptional safety assurance for lithium-ion batteries.

Mechanical Properties

During the assembly, storage, and transportation of lithium-ion batteries (LIBs), separators inevitably undergo deformation from external forces and must withstand repeated electrode volume fluctuations (*e.g.*, graphite negative electrode) during cycling without failure. Consequently, flexibility and shape recovery capability represent important performance indicators.[46] Fig. 7(a) illustrates the deformation tolerance of various membranes after successive mechanical manipulations including bending, twisting, wrinkling, and flattening. Commercial PP membranes exhibit severe residual wrinkles after flattening. Pure PAN-12 membranes demonstrate improved shape recovery, though slight creases remain visible after wrinkling. In contrast, PAN-BM composite membranes (PAN-BM-20, PAN-BM-35, PAN-BM-50) display superior deformation tolerance: following 180° bending and severe wrinkling, all PAN-BM membranes fully recover to their initial flat configuration without significant deformation or structural damage. To quantify mechanical properties, tensile stress–strain tests were performed. As shown in Fig. 7(b), both pure PAN and PAN/BM composite membranes exhibit a monotonic decline in mechanical performance with compositional change. The pure PAN-12 membrane delivers the best overall properties, with a tensile strength of 8.31 MPa and an elongation at break of 44.2%. When the PAN concentration rises to 14% and 16%, the elevated viscosity of the spinning solution causes excessive jet stretching, reduced fiber diameter and fracture defects; strength consequently falls to 7.39 MPa and 6.35 MPa, and elongation at break drops to 35.7% and 26.8%, respectively.

Upon introducing 2 wt%–6 wt% BM into the 12% PAN matrix, the composites show a similar trend. PAN-BM-20 achieves an elongation of 39.6% and a strength of 7.19 MPa, PAN-BM-35 reaches 7.90 MPa and 32.2% and PAN-BM-50 records 6.87 MPa and 27.6%. Although these values are slightly below those of pure PAN-12, the PAN-BM-35 membrane retains about 95% of the pure membrane's strength while exhibiting markedly reduced fiber diameter and increased specific surface area. This indicates that moderate BM loading (≤4%) can refine fiber morphology without severely compromising mechanical integrity.

At 50 wt% BM, however, fiber refinement becomes excessive: the diameter falls below a critical threshold, the cross-sectional area of individual fibers shrinks significantly and their load-bearing capacity drops. Over-stretching during electrospinning also induces partial fiber fracture, creating structural defects. Consequently, PAN-BM-50 fails not because of BM itself but because the overly refined fiber network ruptures fiber-by-fiber under low load. These results demonstrate that BM content must be controlled within a moderate range (≤4%) to balance fiber fineness against mechanical robustness.

Cycle and Rate Performance

Fig. 8 demonstrates that rate capability and cycling performance directly reflect separator adaptability under practical operating conditions.[47] Fig. 8(a) reveals that the PAN-BM-35 separator battery delivers the highest discharge capacity across various current density (*i.e.*, 0.2 C, 0.5 C, 1.0 C, 2.0 C, and return to 0.2 C): an initial capacity of 146.1 mAh/g at 0.2 C, maintaining the capacity of 114.9 mAh/g at the high rate of 2.0 C, with capacity recovering to near-initial values upon returning to 0.2 C. In contrast, the Celgard 2400 and PAN-12 separators exhibit capacities of merely 95.8 mAh/g and 104.1 mAh/g at 2.0 C, respectively. This indicates that the low interfacial impedance and high ion conductivity of PAN-BM-35 effectively mitigate rate polarization and enhance ion transport efficiency at elevated current densities. This exceptional performance stems from BM doping, which optimizes ion transport, interfacial stability, and thermal properties of the membrane, thereby suppressing electrolyte decomposition and electrode side reactions—consistent with the findings of Gao *et al.*[48] Experimental results demonstrate that the low interfacial resistance and high ionic conductivity of PAN-BM-35 effectively mitigate rate polarization and enhance ion transport efficiency under high current densities.

Long-term cycling performance is presented in Fig. 8(b). After 100 cycles at a rate of 0.5 C, the Celgard PP separator decay from 131.2 mAh/g to 95.7 mAh/g (72.9% capacity retention), with fluctuating Coulombic efficiency in later cycles. The PAN-12 membrane decreases from 136.2 mAh/g to 106.4 mAh/g (78.1% capacity retention). The PAN-BM-35 separator, however, maintains superior stability, decreasing from 140.6 mAh/g to approximately 124.2 mAh/g (88.3% capacity retention) with stable Coulomb efficiency exceeding 98%. This exceptional performance arises from the interfacial stability and thermal stability optimized through BM doping, which effectively suppresses electrolyte decomposition and electrode

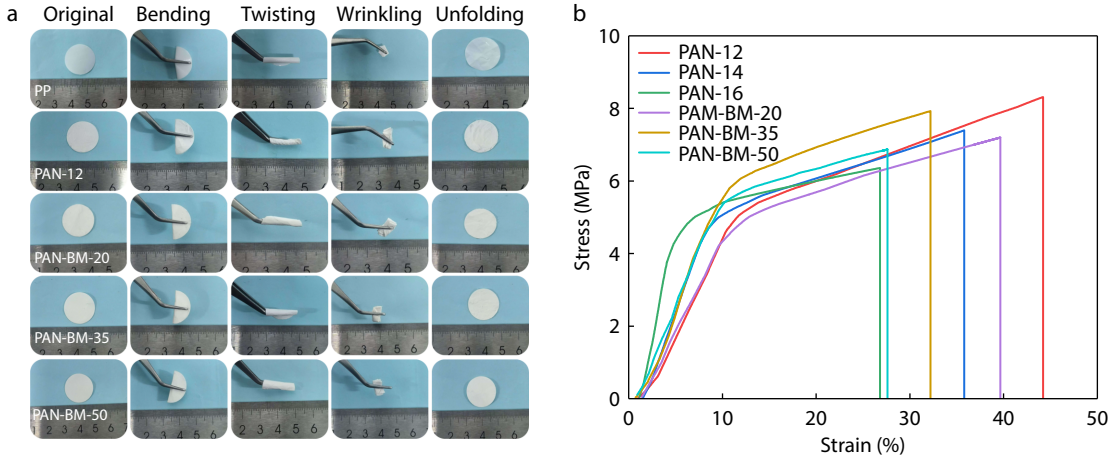

Fig. 7 (a) Deformation recovery capability of commercial PP, PAN-12 and PAN-BM-*x* (*x*=20, 35, 50) electrospun nanofiber membranes (ENSs), and (b) stress-strain curves.

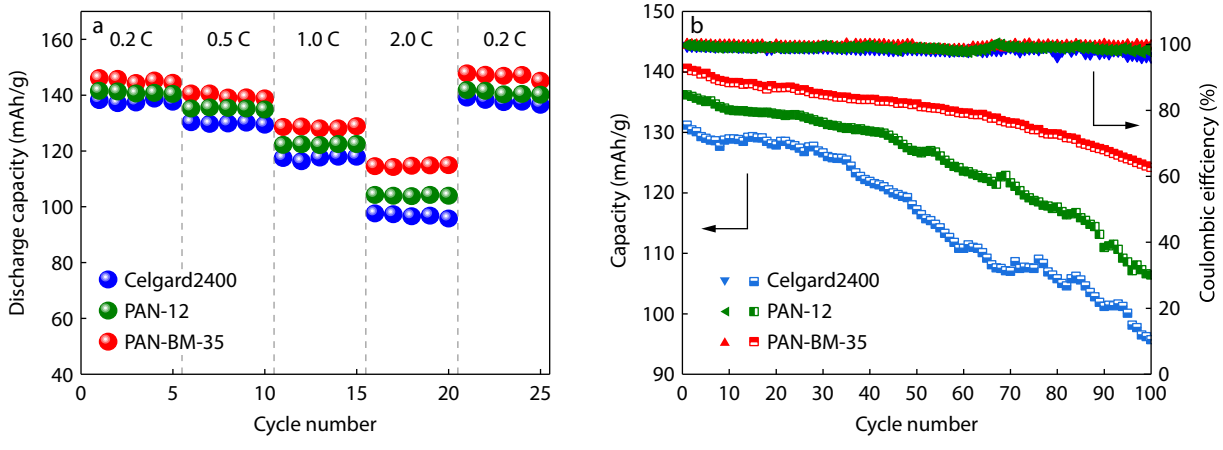

Fig. 8 (a) Cycling performance and (b) rate capabilities of $LiFePO_4$/separator/Li cells with different separators.

https://doi.org/10.1007/s10118-026-3751-1

Table 2 Comparison of key performance parameters between the PAN-BM-35 membrane prepared in this work and representative BM-modified membranes reported in the literature.

Material	Processing method	Porosity (%)	Electrolyte uptake (%)	Dimensionally stable temperature (°C)	Tensile strength (MPa)	Ionic conductivity (mS/cm)	Cycling performance (capacity retention)	Battery (cathode/anode)	Ref.
PAN@PVDF-HFP/BM (PPHB)	Coaxial electrospinning	85.2	872.8	160	5.80	3.98	93.3% after 200 cycles at 0.2 C	LiFePO4/Li	[20]
SDS-Boehmite/PVDF/PEI	Coaxial electrospinning + dip-coating with SDS	about 46	113.6	300	4.27	about 1.0	97.4% after 120 cycles at 0.5 C	LiFePO4/Li	[36]
AlOOH-coated PE	Roller coating (double-faced)	/	/	180	92.70	6.56	96.3% after 100 cycles at 1.0 C	$Li_4T_5O_{12}$/Li	[39]
BM_{220}/PAN	Electrospinning	77.0	660.0	200	8.00	4.46	about 100% after 120 cycles at 1.0 C	LiFePO4/Li	[48]
PAN/BM	Electrospinning	80.7	692.5	200	7.90	3.31	88.3% after 100 cycles at 0.5 C	$LiFePO_4$/Li	This work

side reactions, thereby reducing capacity decay.[49] Based on the comprehensive electrochemical and thermal characterization results, the 12 wt% PAN matrix with 35 wt% BM doping achieves outstanding rate capability and cycling stability through the synergistic effects of high ion conductivity, low interfacial impedance, and excellent thermal stability, providing reliable assurance for the practical lithium-ion batteries applications.

Table 2 compares the key performance parameters of the PAN-BM-35 membrane prepared in this work with representative boehmite-modified separators reported in recent literature. The PAN/BM composite membrane demonstrates competitive advantages across multiple metrics. Its porosity (80.7%) and electrolyte uptake (692.5%) substantially exceed those of AlOOH/PE membranes fabricated by conventional coating processes and surpass several coaxial electrospinning systems. Thermally, the membrane retains structural integrity at 200 °C, matching the BM_{220}/PAN system and outperforming PPHB (160 °C). The ionic conductivity of 3.31 mS/cm ranks above average among comparable materials, while cycling stability (88.3% capacity retention after 100 cycles) is also competitive. Notably, the tensile strength of 7.9 MPa exceeds that of SDS-boehmite/PVDF/PEI (4.27 MPa) and PPHB (5.8 MPa) coaxial systems, and approaches the BM_{220}/PAN value (8.0 MPa). In summary, the PAN-BM-4 membrane achieves a balanced combination of pore architecture, electrolyte affinity and thermal stability, indicating its potential as a high-safety separator for lithium-ion batteries.

CONCLUSIONS

Polyacrylonitrile (PAN)-based composite separators were fabricated by electrospinning, and the effects of PAN concentration and boehmite (BM) doping on separator microstructure and performance were systematically investigated in this study. The results indicate that 12 wt% PAN is the optimal matrix concentration, yielding smooth, bead-free fibers that form a continuous, uniform three-dimensional porous network without interfiber adhesion. Among the BM-doped composites, PAN-BM-35 delivers the best overall performance. In terms of interface performance, the electrolyte uptake of 692.5%, porosity of 80.7% and a contact angle of 25.5° ensure rapid, complete electrolyte infiltration. In terms of mechanical properties, the PAN-BM-35 membrane exhibits a tensile strength of 7.9 MPa, comparable to that of the pure PAN-12 membrane (8.31 MPa), while its elongation at break is 27%, lower than the 44.2% of the pure PAN-12 membrane. Although ductility is reduced, the PAN-BM-35 membrane retains sufficient mechanical integrity to meet the basic requirements for lithium-ion battery assembly. In terms of electrochemical properties, the ionic conductivity of 3.31 mS/cm, interfacial impedance as low as 87 Ω, electrochemical stability window exceeding 5.5 V (versus Li^+/Li), and a lithium-ion transference number (t_{Li^+}) of 0.42, which was substantially higher than that of commercial PP (0.28) and pure PAN-12 (0.34), confirming that BM introduction enhances selective Li^+ transport. The assembled half-cell delivers a discharge capacity of 114.9 mAh/g at 2.0 C, with only 11.7% capacity fade after 100 cycles at 0.5 C and a stable coulombic efficiency above 98%. In terms of thermal safety performance, the separator exhibits negligible shrinkage at 200 °C and a residual mass of 57.6% at 800 °C, and the longest combustion-delay time among all tested samples, significantly outperforming commercial PP separators. Those outstanding performances gain arise from a possible synergistic mechanism, and that is BM surface hydroxyl groups (—OH) hydrogen-bond with PF_6^- anions, suppressing anion migration and promoting selective Li^+ transport. This chemical selectivity, combined with the high porosity and electrolyte affinity of the three-dimensional nanofiber network, achieves concurrent optimization of high ionic conductivity, low interfacial impedance, superior thermal stability and long cycle life. These findings provide a feasible materials strategy and theoretical foundation for the development of next-generation high-performance, high-safety lithium-ion battery separators.

Conflict of Interests

The authors declare no interest conflict.

Electronic Supplementary Information

Electronic supplementary information (ESI) is available free of charge in the online version of this article at http://doi.org/10.1007/s10118-026-3751-1.

Data Availability Statement

The date in this study can be available from the authors uopn reasonable reasons.

REFERENCES

1 Zeng, Z.; Dong, Y.; Yuan, S.; Zhao, W.; Wang, L.; Liu, S.; Yang, Y.; Ge, P.; Sun, W.; Ji, X. Natural mineral compounds in energy-storage systems: development, challenges, prospects. *Energy Storage Mater.* **2022**, *45*, 442–464.

2 Lingappan, N.; Lee, W.; Passerini, S.; Pecht, M. A comprehensive review of separator membranes in lithium-ion batteries. *Renew. Sustain. Energy Rev.* **2023**, *187*, 113726.

3 Yu, Y.; Liu, M.; Chen, Z.; Zhang, Z.; Qiu, T.; Hu, Z.; Xiang, H.; Zhu, L.; Xu, G.; Zhu, M. Advances in nonwoven-based separators for lithium-ion batteries. *Adv. Fiber Mater.* **2023**, *5*, 1827–1851.

4 Lagadec, M. F.; Zahn, R.; Wood, V. Characterization and performance evaluation of lithium-ion battery separators. *Nat. Energy* **2019**, *4*, 16–25.

5 Liu, J. H.; Wang, P.; Gao, Z.; Li, X. Review on electrospinning anode and separators for lithium ion batteries. *Renew. Sustain. Energy Rev.* **2024**, *189*, 113939.

6 Wang, Y.; Zhuang, W.; Bian, H.; Yang, B.; Bin, D.; Shi, J.; Lu, H. Lithium-ion battery separator using inorganic materials: a mini review. *J. Power Sources* **2025**, *643*, 237015.

7 Jiang, Y.; Ding, Y.; Zhang, P.; Li, F.; Yang, Z. Temperature-dependent on/off PVP@TiO_2 separator for safe Li-storage. *J. Membr. Sci.* **2018**, *565*, 33–41.

8 Shi, C.; Zhang, P.; Huang, S.; He, X.; Yang, P.; Wu, D.; Zhao, J. Functional separator consisted of polyimide nonwoven fabrics and polyethylene coating layer for lithium-ion batteries. *J. Power Sources* **2015**, *298*, 158–165.

9 Wu, D.; Shi, C.; Huang, S.; Qiu, X.; Wang, H.; Zhan, Z.; Lin, L. Electrospun nanofibers for sandwiched polyimide/poly(vinylidene fluoride)/polyimide separators with the thermal shutdown function. *Electrochim. Acta* **2015**, *176*,

Graphical Abstract

Boehmite/Polyacrylonitrile Composite Nanofiber Separator with Enhanced Ionic Conductivity and Thermal Stability for Lithium-Ion Batteries

Zhi-Jun Tu, Sheng-Bin Cao, Xiao-Song Liu, Xiao-Peng Li, Wei Luo, and Dávid István Kis

Shanghai Dianji University, China; Oxford Suzhou Centre for Advanced Research, China; Donghua University, China; John von Neumann University, Hungary

This work employed electrospinning technology to construct a novel Boehmite/polyacrylonitrile (BM/PAN) composite nanofiber separator and investigated the effects of varying BM content on the separator's structure and electrochemical performance.

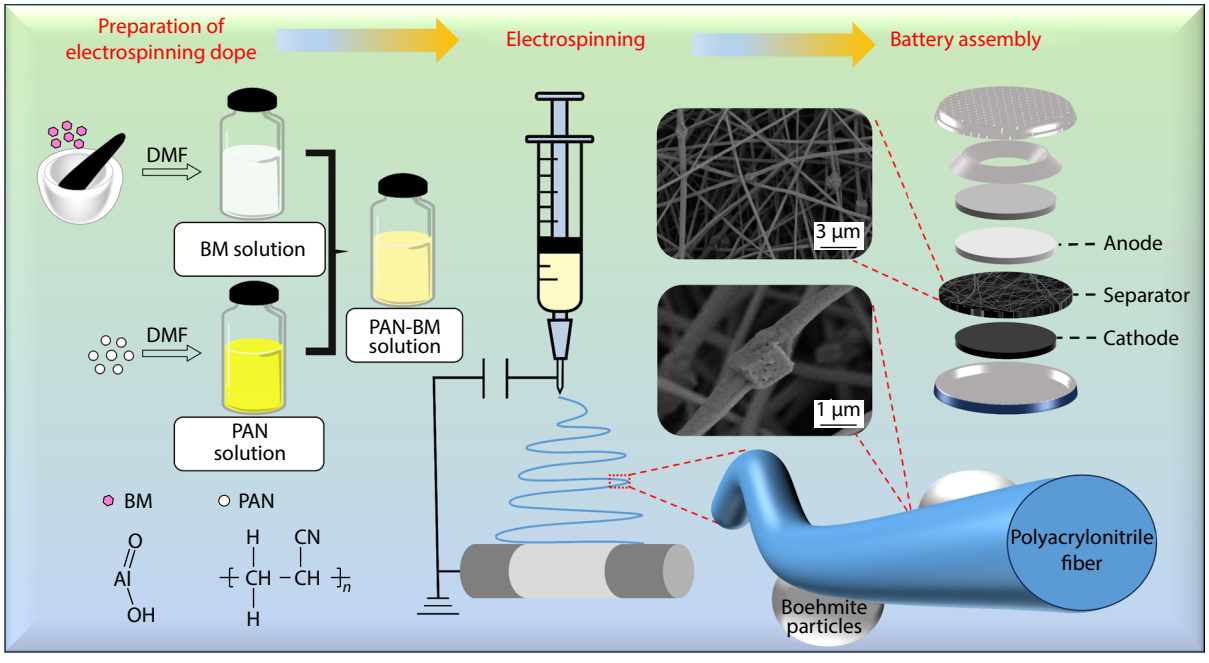

Chinese J. Polym. Sci., 2026 *https://doi.org/10.1007/s10118-026-3751-1*

727–734.
10 Sun, G.; Liu, B.; Niu, H.; Hao, F.; Chen, N.; Zhang, M.; Wu, D. In situ welding: superb strength, good wettability and fire resistance tri-layer separator with shutdown function for high-safety lithium ion battery. *J. Membr. Sci.* **2020**, *595*, 117509.
11 Wang, K.; Wang, W.; Wang, Y.; Wang, M. Dual phase change separator combining cooling and thermal shutdown functions for Li-ion battery with enhanced safety. *Chem. Eng. J.* **2024**, *481*, 148538.
12 Zheng, G.; Zeng, Z.; Shao, Z.; Shen, R.; Li, H.; Jiang, J.; Liu, Y. Coaxial electrospun core-shell lithium-ion battery separator with flame retardant and thermal shutdown functions. *Mater. Chem. Phys.* **2023**, *301*, 127647.
13 Kim, T. H.; Kim, M.; Kim, E. J.; Ju, M.; Kim, J. S.; Lee, S. H. Highly stretchable thermoplastic polyurethane separators for Li-ion batteries based on non-solvent-induced phase separation method. *Polymers* **2024**, *16*, 357.
14 Zhu, H.; Dong, B.; Cai, X.; Xi, L.; Zhang, P.; Hao, Y.; Zeng, R. In situ covalent crosslinking strategy to construct highly stable composite separators for lithium-ion batteries. *Chem. Eng. J.* **2024**, *488*, 151120.
15 Tang, W.; Liu, Q.; Luo, N.; Chen, F.; Fu, Q. High safety and electrochemical performance electrospun para-aramid nanofiber composite separator for lithium-ion battery. *Compos. Sci. Technol.* **2022**, *225*, 109479.
16 He, J.; Yang, L.; Ruan, X.; Liu, Z.; Liao, K.; Duan, Q.; Zhan, Y. Electrospun PVDF-based polymers for lithium-ion battery separators: a review. *Polymers* **2024**, *16*, 2895.
17 Cai, M.; Yuan, D.; Zhang, X.; Pu, Y.; Liu, X.; He, H.; Ning, X. Lithium ion battery separator with improved performance *via* side-by-side bicomponent electrospinning of PVDF-HFP/PI followed by 3D thermal crosslinking. *J. Power Sources* **2020**, *461*, 228123.
18 Chen, Y.; Song, Z.; Liu, H.; Xu, H.; Xi, Y.; Yin, C.; Zhou, L. Cross-linking synergistic effects to enhance the comprehensive properties of electrospun polyimide nanofiber membranes for advanced lithium-ion batteries. *ACS Sustainable Chem. Eng.* **2024**, *12*, 5953–5964.
19 Gong, W.; Zhang, Z.; Wei, S.; Ruan, S.; Shen, C.; Turng, L. S. Thermosensitive polyacrylonitrile/polyethylene oxide/polyacrylonitrile membrane separators for prompt and safer thermal lithium-ion battery shutdown. *J. Electrochem. Soc.* **2020**, *167*, 020509.
20 Chen, Z.; Guan, M.; Cheng, Y.; Li, H.; Ji, G.; Chen, H.; Wu, C. Boehmite-enhanced poly(vinylidene fluoride-co-hexafluoropropylene)/polyacrylonitrile (PVDF-HFP/PAN) coaxial electrospun nanofiber hybrid membrane: a superior separator for lithium-ion batteries. *Adv. Compos. Hybrid Mater.* **2023**, *6*, 219.
21 Li, Y.; Pan, C.; Gan, F.; Lin, Z. X.; Yu, J. C.; Wei, Z. Z.; Zhao, Y. Robust composite separator randomly interwoven by PI and pre-oxidized PAN nanofibers for high performance lithium-ion batteries. *Chinese J. Polym. Sci.* **2024**, *42*, 1768–1779.
22 Wang, Y.; Wang, Q.; Wei, X.; Song, Z.; Lan, Y.; Luo, W.; Li, X. A novel three-dimensional boehmite nanowhiskers network-coated polyethylene separator for lithium-ion batteries. *Ceram. Int.* **2021**, *47*, 10153–10162.
23 Li, X.; Chen, S.; Xia, Z.; Li, L.; Yuan, W. High performance of boehmite/polyacrylonitrile composite nanofiber membrane for polymer lithium-ion battery. *RSC Adv.* **2020**, *10*, 27492–27501.
24 Jafaripour, H.; Sanaee, Z.; Mahdavi, H. Polymer-less electrospinning for realization of silica nanofibers membrane as a flexible separator with ultra-high electrolyte uptake, for high safety lithium ion batteries. *J. Power Sources* **2025**, *631*, 236237.
25 Nien, Y. H.; Chang, C. N.; Chuang, P. L.; Hsu, C. H.; Liao, J. L.; Lee, C. K. Fabrication and characterization of nylon 66/PAN nanofibrous film used as separator of lithium-ion battery. *Polymers* **2021**, *13*, 1984.
26 Wang, X.; Cui, X.; He, B.; Zhao, Q.; Wang, Y.; Xiao, D.; Li, K. A high-safety lithium-ion battery electrospun separator with Si_3N_4-assisted sulfonated poly(ether ether ketone) for regulating lithium flux. *J. Colloid Interface Sci.* **2025**, *678*, 460–471.
27 Wang, J.; Sun, X.; Sun, X.; He, C.; Li, L.; Wang, W.; Huang, Y. Superior and safer lithium-ion batteries enabled by electrospun poly(m-phenylene isophthalamide)-based separator with high heat resistance and flame retardance. *J. Energy Storage* **2025**, *137*, 118697.
28 Li, H.; Feng, T.; Liang, Y.; Wu, M. Construction of PMIA@PAN/PVDF-HFP/TiO_2 coaxial fibrous separator with enhanced mechanical strength and electrolyte affinity for lithium-ion batteries. *Chin. Chem. Lett.* **2023**, *34*, 108350.
29 Gu, J. P.; Zhang, K. Y.; Li, X. T.; Dong, J.; Zhang, Q. H.; Zhao, X. Construction of Safety and Non-Flammable Polyimide Separator Containing Carboxyl Groups for Advanced Fast Charging Lithium-Ion Batteries. *Chinese J. Polym. Sci.* **2022**, *40*, 345–354.
30 Al-Okaidy, H. S.; Waisi, B. I. The effect of electrospinning parameters on morphological and mechanical properties of PAN-based nanofibers membrane. *Baghdad Sci. J.* **2023**, *20*, 1433–1433.
31 Shayapat, J.; Chung, O. H.; Park, J. S. Electrospun polyimide-composite separator for lithium-ion batteries. *Electrochim. Acta* **2015**, *170*, 110–121.
32 Meera, K.; Ramesan, M. T. Tailoring the performance of boehmite nanoparticles reinforced carboxymethyl chitosan/cashew gum blend nanocomposites *via* green synthesis. *Polymer* **2023**, *268*, 125706.
33 Kirecci, A.; Özkoç, Ü.; İçoğlu, H. İ. Determination of optimal production parameters for polyacrylonitrile nanofibers. *J. Appl. Polym. Sci.* **2012**, *124*, 4961–4968.
34 Habeeb, S. A.; Rajabi, L.; Dabirian, F. Production of polyacrylonitrile/boehmite nanofibrous composite tubular structures by opposite-charge electrospinning with enhanced properties from a low-concentration polymer solution. *Polym. Compos.* **2020**, *41*, 1649–1661.
35 Guo, M.; Zhu, H.; Wan, P.; Xu, F.; Wang, C.; Lu, S.; Xu, J. Freestanding and ultra-flexible PAN/ZIF-67 hybrid membrane with controlled porosity for high-performance and high-safety lithium batteries separator. *Adv. Fiber Mater.* **2022**, *4*, 1511–1524.
36 Chen, X.; Yu, Z.; Cui, W.; Ding, Y.; Wu, J.; Hou, Y.; Gong, G. Surfactant-Enabled BM particle-embedded coaxial PVDF/PEI electrospun membranes enhancing Lithium-Ion battery safety. *Chem. Eng. J.* **2025**, *503*, 158225.
37 Szewczyk, P. K.; Ura, D. P.; Metwally, S.; Knapczyk-Korczak, J.; Gajek, M.; Marzec, M. M.; Stachewicz, U. Roughness and fiber fraction dominated wetting of electrospun fiber-based porous meshes. *Polymers* **2018**, *11*, 34.
38 Gong, X.; Xiao, Q.; Li, Q. Y.; Liang, W. C.; Chen, F.; Li, L. Y.; Ren, S. J. Cross-linked electrospun gel polymer electrolytes for lithium-ion batteries. *Chinese J. Polym. Sci.* **2024**, *42*, 1021–1028.
39 Yang, C.; Tong, H.; Luo, C.; Yuan, S.; Chen, G.; Yang, Y. Boehmite particle coating modified microporous polyethylene membrane: A promising separator for lithium ion batteries. *J. Power Sources* **2017**, *348*, 80–86.
40 Choi, E. S.; Lee, S. Y. Particle size-dependent, tunable porous structure of a SiO_2/poly(vinylidene fluoride-hexafluoropropylene)-coated poly(ethylene terephthalate) nonwoven composite separator for a lithium-ion battery. *J. Mater. Chem.* **2011**, *21*, 14747–14754.
41 Luo, Z.; Lin, Z.; Lu, J.; Zhang, D.; Li, Y.; Liu, L.; Liu, D. Hydrogen-bonding mesoporous boehmite orchestrating anion-derived solvation regulation and confinement toward dendrite-free lithium anodes. *Adv. Compos. Hybrid Mater.* **2026**, *9*, 70.

42 Yu, J.; Dong, N.; Liu, B.; Tian, G.; Qi, S.; Wu, D. A newly-developed heat-resistance polyimide microsphere coating to enhance the thermal stability of commercial polyolefin separators for advanced lithium-ion battery. *Chem. Eng. J.* **2022**, *442*, 136314.
43 Lee, J. H.; Nathan, M. G. T.; Kim, H. W.; Lee, S. M.; Kim, H. I.; Kim, J. H.; Kim, J. K. A High-stable polyacrylonitrile/ceramic composite membranes for high-voltage lithium-ion batteries. *Mater. Chem. Phys.* **2022**, *291*, 126516.
44 Ding, W.; Liu, Y.; Xu, L. Batch preparation and performance study of boehmite-based electrospun nanofiber separators for lithium-ion batteries. *Molecules* **2024**, *29*, 3938.
45 Peng, F.; Jiang, Y.; Liu, F.; Feng, J.; Feng, J.; Li, L. Hydrothermal assisted synthesis of heat resistant, well-crystallized aerogels constructed by boehmite nano rods. *Ceram. Int.* **2022**, *48*, 16232–16240.
46 Deng, J.; Cao, D.; Yang, X.; Zhang, G. Cross-linked cellulose/carboxylated polyimide nanofiber separator for lithium-ion battery application. *Chem. Eng. J.* **2022**, *433*, 133934.
47 Hou, Y.; Huang, Z.; Chen, Z.; Li, X.; Chen, A.; Li, P.; Zhi, C. Bifunctional separators design for safe lithium-ion batteries: Suppressed lithium dendrites and fire retardance. *Nano Energy* **2022**, *97*, 107204.
48 Gao, T.; Tian, P.; Xu, Q.; Pang, H.; Ye, J.; Ning, G. Class of boehmite/polyacrylonitrile membranes with different thermal shutdown temperatures for high-performance lithium-ion batteries. *ACS Appl. Mater. Interfaces* **2022**, *15*, 2112–2123.
49 Yanilmaz, M.; Lu, Y.; Dirican, M.; Fu, K.; Zhang, X. Nanoparticle-on-nanofiber hybrid membrane separators for lithium-ion batteries *via* combining electrospraying and electrospinning techniques. *J. Membr. Sci.* **2014**, *456*, 57–65.